

“Atlas” of numerical solutions for star-disk magnetospheric interaction

M. Čemeljić

Nicolaus Copernicus Astronomical Center, Bartycka 18, 00-716 Warsaw, Poland e-mail: miki@camk.edu.pl

Received ??; accepted ??

ABSTRACT

Aims. I report results in numerical simulations of star-disk magnetospheric interaction. A thin accretion disk with corona above a rotating stellar surface is simulated in a parameter study, to find trends in the angular momentum flux. The results are presented in the case of Young Stellar Objects, but they can be rescaled to other objects with similar geometry.

Methods. In the performed resistive and viscous magneto-hydrodynamic simulations, a quasi-stationary state is reached in the cases with different parameters. Angular momentum fluxes in the different components of the flow are computed, to compare the results.

Results. Results in the simulations are presented with the matter density distribution and magnetic field geometry displayed in an “Atlas” of solutions. The torque exerted on the star is computed, together with the angular momentum flux loaded into outflow, in the cases when a conical outflow is formed. In the studied part of the parameter space, I find trends in both components of the flow.

Key words. Stars: formation, pre-main sequence, – magnetic fields –MHD

1. Introduction

An analytical solution for viscous accretion disk has been given in Shakura & Sunyaev (1973), few years after the first numerical solution by Prendergast and Burbidge (1968). As in many numerical and analytical models which followed, the disk structure was derived separately in radial and vertical direction. The radial structure was computed by equations averaged over the disk thickness, and the vertical structure from the hydrostatic equilibrium in the vertical direction. In some models, the radiative transfer was also taken into account.

Height-averaged computations were shown to be insufficient in the analytical work by Urpin (1984), and also in many numerical works, starting with Kley and Lin (1992). In all of them, a backflow in the disk midplane occurs, thought to be of thermal origin.

A thin accretion disk analytical solution in three dimensions has been given in (Kluźniak & Kita 2000, hereafter KK00). They derived the equations of polytropic, viscous hydrodynamical accretion disk, using the Taylor expansion in the small parameter $\epsilon = H/R$, the disk aspect ratio. In spite of neglecting the thermal effects, backflow is still present with the values of the viscosity parameter $\alpha_v < 0.685$. Such a disk accretes only at the higher latitudes, closer to the surface, with the backflow in the mid-plane occurring at a particular distance from the star. Inside this distance, the matter is always flowing towards the star. If $\alpha_v > 0.685$, the disk accretes across the entire height.

With the stellar magnetic field and disk resistivity added in the model, angular momentum transfer depends on the details of star-disk magnetospheric interaction. As first shown in Ghosh & Lamb (1979a,b), to correctly describe this interaction, it is not enough to consider only the disk. The rotating stellar surface and corona have to be included in the model, to include the interaction with the region in the disk below, and beyond the corotation radius. Pioneering such simulations were Romanova et al. (2009, 2013) and Zanni & Ferreira (2009, 2013). As mentioned in (Zanni & Ferreira 2009, hereafter ZF09), for closing on the answer to stellar angular momentum problem, the different regimes of magnetospheric interaction should be probed, through the exploration of the parameter space. Here I follow this suggestion.

In §2 I demonstrate the difference in geometry in the results with different parameters, obtained from a set of simulations sweeping through the parameter space. In §3 the results with different parameters in the simulations are compared, and trends illustrated, with conclusions listed in §4. A short but detailed technical exposition of the code set-up, and an “Atlas” of quasi-stationary states in all the simulations are presented in Appendix.

2. Simulations of star-disk magnetospheric interaction

Using the PLUTO code (v.4.1) (Mignone et al. 2007, 2012), I perform simulations of star-disk magnetospheric interaction (SDMI). Initial conditions in the disk and corona, and boundary conditions at the edges of the computational do-

Send offprint requests to: M. Čemeljić

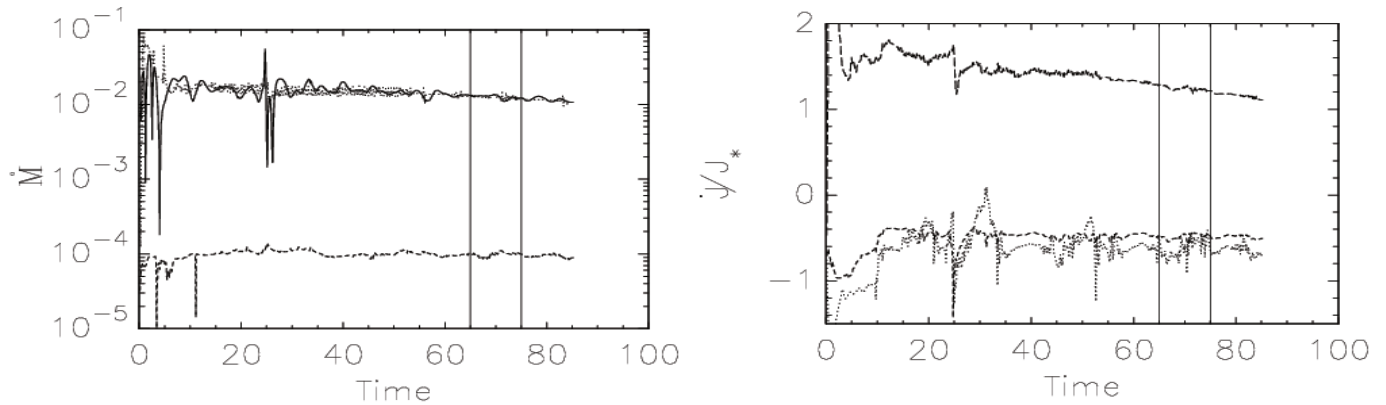


Fig. 1. Fluxes in the result in a case with $\Omega_\star = 0.1\Omega_{\text{br}}$, $B_\star = 0.5$ kG, $\alpha_m = 1$. In the left panel, with solid, dotted and dashed lines is shown the mass flux across the disk at $R=12R_\star$, onto the star and into the stellar wind, respectively. In the right panel, angular momentum flux of the matter in-falling onto the star from the distances below and beyond the corotation radius is shown with the long and short dashed lines, respectively, and in the stellar wind with the dotted line. Vertical solid lines mark the interval in time, in which is taken an average for computation of the quasi-stationary state.

Table 1. Parameter space in the study presented in “Atlas”: the stellar angular velocity Ω_\star , stellar dipole magnetic field strength B_\star , and the magnetic Prandtl number P_m for which the also given the values of corresponding resistivity parameter α_m . Shown are the stellar rotation period and corotation radius in young stellar object (YSO) cases.

$\Omega_\star/\Omega_{\text{br}}$	$B_\star(\text{G})$	P_m	α_m	$P_\star(\text{days})$	$R_{\text{cor}}(R_\star)$
0.05	250	6.7	0.1	9.2	7.37
0.1	500	1.67	0.4	4.6	4.64
0.15	750	0.95	0.7	3.1	3.54
0.2	1000	0.67	1.0	2.3	2.92

main closely follow ZF09. See Appendix A for the details of numerical set-up.

Simulations span over 64 points in the parameter space (see Table 1), by varying stellar angular velocity Ω_\star , expressed in the units of stellar breakup angular velocity $\Omega_{\text{br}} = \sqrt{GM_\star/R_\star^3}$, stellar magnetic field strength B_\star , and the magnetic Prandtl number

$$P_m = \frac{2}{3} \frac{\alpha_v}{\alpha_m}, \quad (1)$$

where α_m is the resistive parameter. In the simulations presented here, I fixed viscosity parameter to $\alpha_v = 1$.

To compare the results in the different points in the parameter space, a quasi-stationary state in each of the simulations is found. I rely on two measurements: of the mass flux \dot{M} and the angular momentum flux \dot{J} .

The fluxes are computed by integrating

$$\dot{M} = \int_S \rho \mathbf{v}_p \cdot d\mathbf{S}, \quad \dot{J} = \int_S \left(r \rho v_\varphi \mathbf{v}_p - \frac{r B_\varphi \mathbf{B}_p}{4\pi} \right) d\mathbf{S},$$

over the corresponding surface \mathbf{S} in the different parts of the flow.

Computed are the mass and angular momentum fluxes onto the star, into the stellar wind, and across the disk height in the middle part of the disk, at $R_d=12R_\star$. In the cases in which an outflow forms, the fluxes loaded into it are also computed at this distance. In the angular momentum flux onto the star, the part coming from beyond, and

below the corotation radius $R_{\text{cor}} = (GM_\star/R_\star^2)^{1/3}$ are computed separately. A sign convention is such that a positive angular momentum flux increases the total in the system, and a negative decreases it. In both fluxes, the equatorial symmetry is taken into account so that fluxes are computed in a complete meridional plane.

A typical example, computed in one point of the parameter space in the simulations, is presented in Fig. 1. It shows that after relaxation from the initial and boundary conditions (lasting typically 10-50 stellar rotations), the quasi-stationary state is reached. Oscillations in the simulations, still present into the quasi-stationary state, are smoothed-out by averaging over some characteristic interval—typically an average is taken over ten stellar rotations. In the example considered here, the averaging interval is from 65 to 75 stellar rotations.

In each of the 64 simulations, such an interval is chosen in which both the mass and angular momentum fluxes are not varying much. Then an average value is found of the angular momentum flux through the various components in the flow during that time interval.

In Appendix B is provided an “Atlas” of results in performed numerical simulations. In each of the cases shown is a snapshot of matter density in the quasi-stationary state, with a sample of magnetic field lines.

Three geometries in the solutions in “Atlas” can be distinguished, shown in Fig. 2:

- Disk connected with the star by an accretion column,
- Disk pushed away from the star, without an accretion column,
- Conical outflow above the accretion column connecting the star and the disk.

Information about the geometry and reach of the stellar magnetic field in the disk is helpful in choosing the physical parameters in the model for the post-processing or further analysis of the results.

3. Trends in the angular momentum flux

After indicating the quasi-stationary states in simulations, I proceed to the comparison of solutions presented in “Atlas”.

In the first example, in Fig. 4 is shown a comparison of density in the middle part of the disk in the simulations

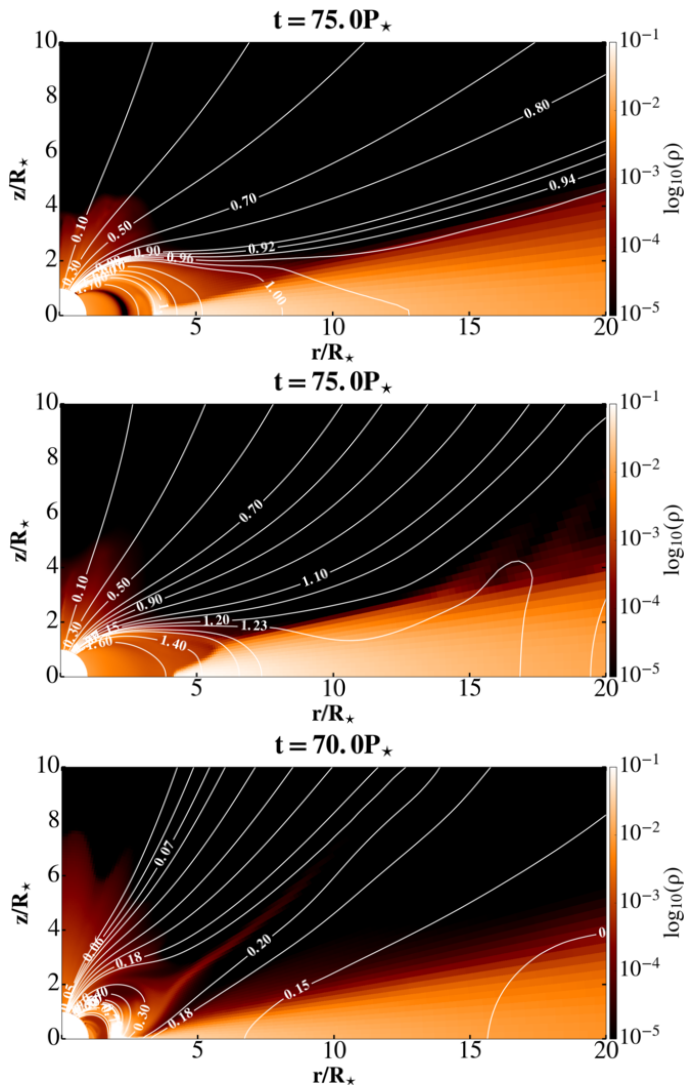


Fig. 2. Three different cases of geometry in the results. In the top and middle panels are shown the matter density and a sample of magnetic field lines, with the stellar magnetic field $B_* = 1$ kG and the resistivity $\alpha_m = 1$, in the cases with the stellar rotation rates $\Omega_* = 0.1\Omega_{br}$ (top panel) where a stable accretion column is formed) and $\Omega_* = 0.15\Omega_{br}$ (middle panel) in which the faster stellar rotation prevents the accretion column formation. In the bottom panel is shown the third case, with stellar magnetic field $B_* = 0.5$ kG, resistivity $\alpha_m = 0.1$ and the rotation rate $\Omega_* = 0.1\Omega_{br}$, in which is formed a conical outflow.

with the increasing stellar magnetic field. The density increases with the increasing magnetic field. This trend will contribute to the trends in mass and angular momentum fluxes.

In the second example, compared are simulations with the increasing stellar rotation rate, in which the stellar magnetic field remains unchanged. Angular momentum flux from the accretion disk loads into various components of the flow: onto the star through the accretion column, into the stellar wind and into the conical outflow, in the cases when it is formed.

By comparing the solutions, I find a trend in the angular momentum flux, shown in Fig. 3. With the increase in the stellar rotation rate, a spin-up of the star by the infalling matter decreases and eventually switches to a spin-down.

A similar outcome is obtained in each of the cases with different stellar magnetic field strengths. Such a trend is not surprising since for slowly rotating stars the torque exerted on the star will depend mostly on the stellar magnetic field, at each value of the resistivity parameter. The trend will change only after a change in geometry of the flow.

The third example of a trend in the results is in the cases with $\alpha_m = 0.1$, in which a conical outflow is formed. The angular momentum flux expelled from the system with such an outflow in the cases with different magnetic field strength is shown in Fig. 5.

The momentum flux in the outflow does not change much, except in the cases with faster stellar rotation *and* large magnetic field, when the outflow takes away much more, for an order of magnitude, of the angular momentum from the system. The magnetospheric ejection increases with the stronger magnetic field and faster rotation.

Trends in the presented examples can be compared with the results in other models and simulations when they become available. If found robust, such trends should be compared with the observations and incorporated in the star formation models.

4. Conclusions

In the numerical simulations of star-disk magnetospheric interaction (SDMI), I investigate angular momentum flux in the system. In a parameter study, stellar rotation rate, magnetic field, and the disk resistivity are varied, to obtain a suite of the quasi-stationary solutions. I compute the angular momentum flux in different components of the flow to compare results in the cases with different stellar magnetic field strengths.

Discussing the results, in the first example I find a trend in the matter density along a vertical line in a mid-part of the disk. The density increases with the increasing stellar magnetic field in the simulation.

The second result is a trend in angular momentum flux onto the star, with the increasing stellar rotation rate. I find that with the faster stellar rotation, spin-up of the star decreases, and eventually switches to a spin-down.

The third find from the performed simulations is that in the cases with $\alpha_m = 0.1$ and a faster rotating star, the angular momentum flux loaded into the conical outflow increases significantly, with the large values of the stellar magnetic field. The increase is for an order of magnitude. In the cases with a small stellar magnetic field, there is no change in a load of angular momentum in the outflow.

The results apply in disks around young stellar objects (YSOs) and can be rescaled to disks in a compact binary. I provide a table with scaling factors for different cases.

I presented here the results with a slowly rotating star. In the simulations with a stellar rotation faster than 20% of the stellar breakup rotation rate, two additional kinds of a solution are obtained, similar to Romanova et al. (2009): with a fast axial outflow, and with both the conical and axial outflow. I leave them for a separate study, together with the solutions with $\alpha_v < 0.685$, which show a backflow in the initial disk.

Acknowledgements

MČ developed the set-up of star-disk simulations while in CEA, Saclay, France, under the ANR Toupies grant with

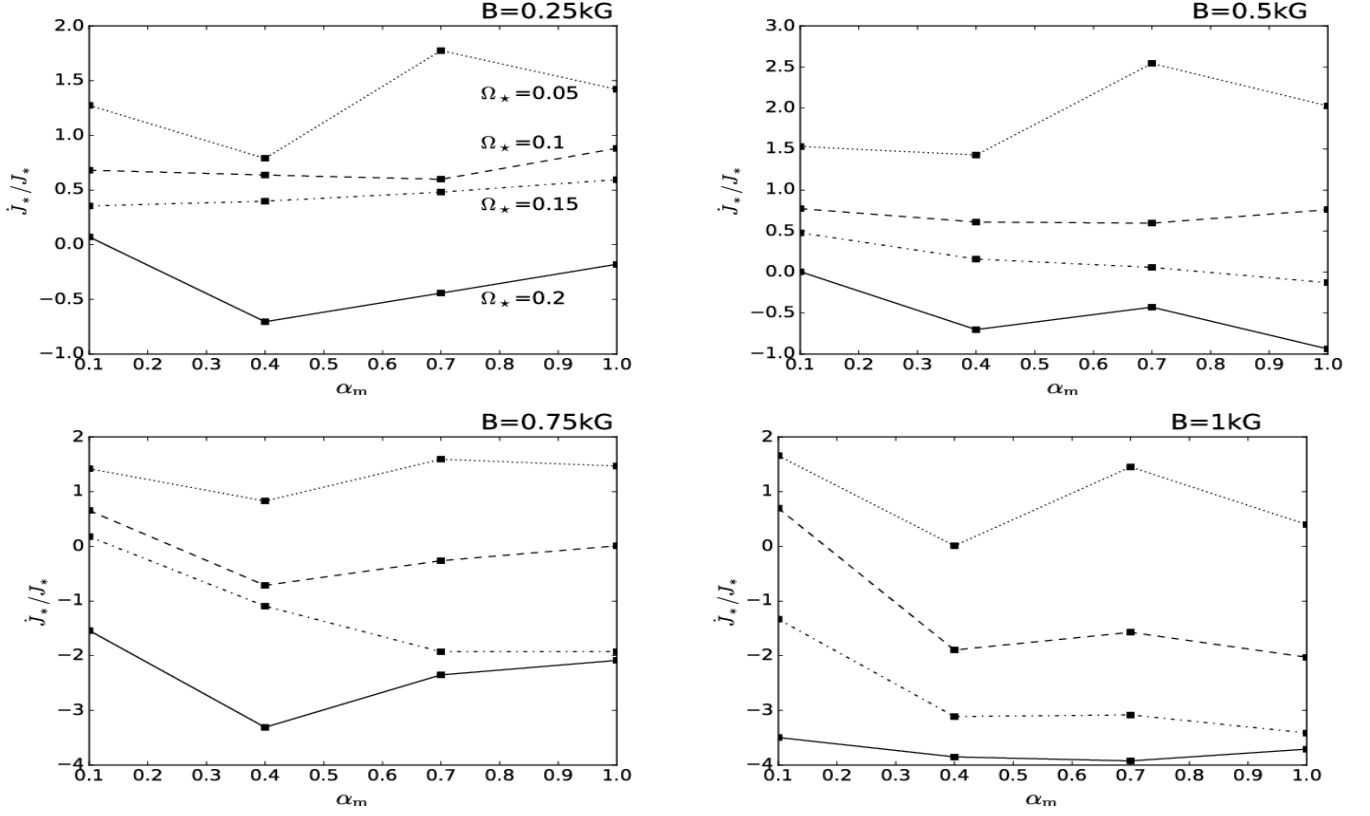


Fig. 3. Average angular momentum flux transported onto the stellar surface by the matter in-falling from the disk onto the star through the accretion column. In each panel is shown a set of solutions with one stellar magnetic field strength, varying the stellar rotation rate and resistivity. Results with $\Omega_*/\Omega_{\text{br}} = 0.05, 0.1, 0.15$ and 0.2 are shown with the dotted, dashed, dash-dot-dot and solid lines, respectively, in the units of stellar angular momentum expressed in $J_{*0} = \rho_{d0} R_*^4 V_{K*}$. Positive flux spins-up the star, negative slows it down. With the increase in stellar rotation rate, spin-up of the star by the infalling matter decreases, eventually switching to the spin-down.

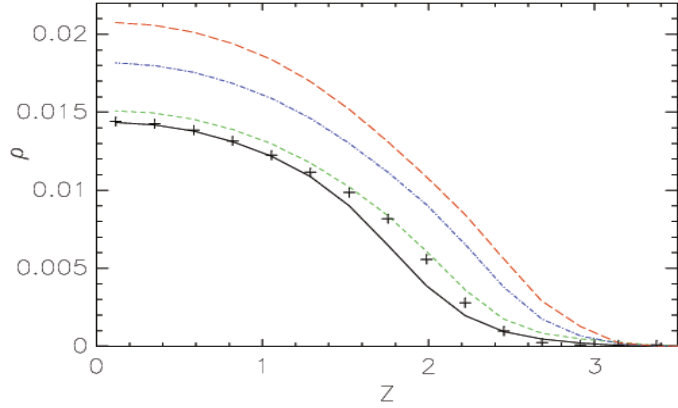


Fig. 4. Disk density in the simulations, measured along the disk height at $R=15R_*$. With solid (black), short-dashed (green), dash-dotted (blue) and long-dashed (red) lines are shown results in the cases with $B_* = 0.25, 0.5, 0.75$ and 1 kG , respectively. There is a trend in density, with the increasing stellar field. Result in the simulations without magnetic field is depicted in plus symbols.

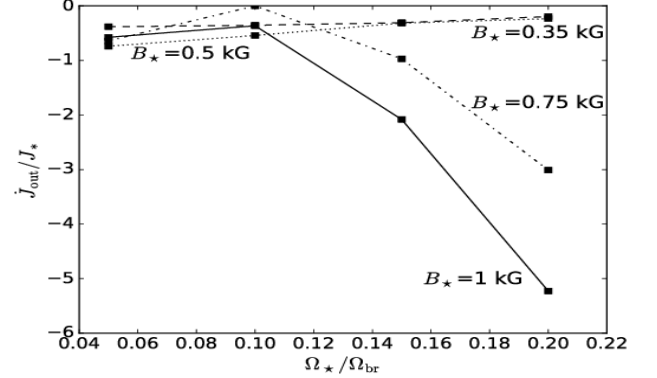


Fig. 5. Average angular momentum flux in the outflow, which forms in the cases with $\alpha_m=0.1$. It is computed at $R=12R_*$, in the cases with different stellar rotation rates. Normalization is to the stellar angular momentum expressed in $J_{*0} = \rho_{d0} R_*^4 V_{K*}$. With dotted, dash-dotted, dashed and solid lines are shown the fluxes in the $B_* = 0.25, 0.5, 0.75$ and 1 kG cases, respectively.

A.S. Brun. Work in NCAC Warsaw is funded by a Polish NCN grant no. 2013/08/A/ST9/00795, and a collaboration with Croatian STARDUST project through HRZZ grant IP-2014-09-8656 is acknowledged. I thank IDRIS (Turing cluster) in Orsay, France, ASIAA/TIARA (PL and XL clus-

ters) in Taipei, Taiwan and NCAC (PSK cluster) in Warsaw, Poland, for access to Linux computer clusters used for the high-performance computations. The PLUTO team is thanked for the possibility to use the code, in particular C. Zanni for help with the code modifications. V. Parthasarathy and F. Bartolić are acknowledged for devel-

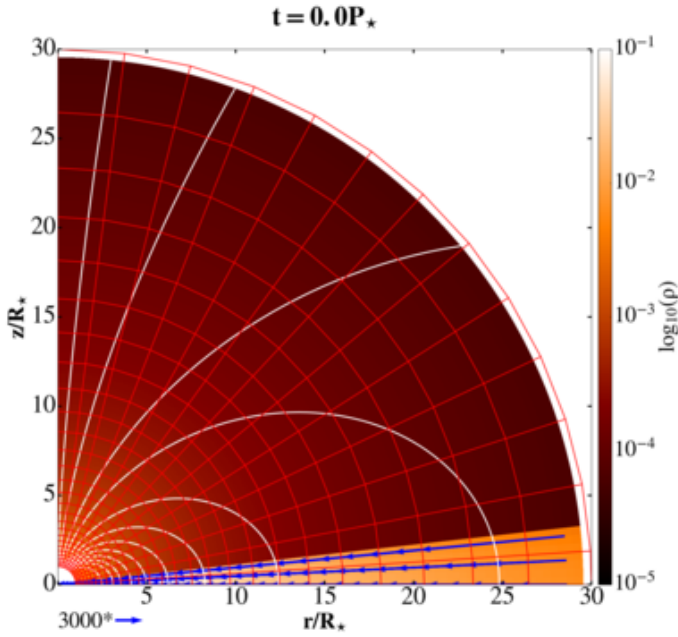


Fig. A.1. The initial density distribution of matter in simulations, with a sample of the initial poloidal magnetic field lines shown with the solid white lines. The vectors show the initial velocity distribution in the disk, with the unit vector length measured in Keplerian velocity units indicated below the figure. The computational grid is shown in 8x8 blocks of cells.

oping the Python scripts for visualization, N. Bessolaz for the initial version of the set-up, and M. Flock for useful discussions about the code.

References

- Čemeljić, M., Parthasarathy, V. & Kluźniak, W., 2017, JPhCS, 932, 012028
- Ghosh, P., & Lamb, F.K., 1979a, ApJ, 232, 259
- Ghosh, P., & Lamb, F.K., 1979b, ApJ, 234, 296
- Kley, W. and Lin, D.N.C., 1992, ApJ397, 600
- Kluźniak, W., Kita, D., 2000, arXiv:astro-ph/0006266
- Mignone, A., Bodo, G., Massaglia, S., Matsakos T., Tesileanu O., Zanni C., Ferrari A., 2007, APJ Series, 170, 228
- Mignone, A., Zanni, C., Tzeferacos, P., van Straalen, B., Colella, P., and Bodo, G., 2012, APJ Series, 198, 7
- Powell, K. G., Roe, P. L., Linde, T. J., Gombosi, T. I., & De Zeeuw, D. L. 1999, J. Comput. Phys, 154, 284
- Prendergast, K.H., Burbidge, G.R., 1968, ApJ, 151, L83
- Romanova, M.M., Ustyugova, G.V., Koldoba, A.V., Lovelace, R.V.E., 2009, MNRAS, 399, 1802
- Romanova, M.M., Ustyugova, G.V., Koldoba, A.V., Lovelace, R.V.E., 2013, MNRAS, 430, 699
- Shakura, N.I., Sunyaev, R.A., 1973, A&A, 24, 337
- Tanaka, T. 1994, J. Comput. Phys., 111, 381
- Urpin, V.A. 1984, Astron. Zh. 61, 84 [Sov. Astron. 28, 50].
- Urpin, V.A. 1984b, Astrophys. Sp. Sci. 90, 79.
- Zanni, C., Ferreira, J., 2009, A&A, 512, 1117
- Zanni, C., Ferreira, J., 2013, A&A, 550, A99

Appendix A: Numerical simulations of star-disk magnetospheric interaction

Star-disk magnetospheric interaction (SDMI) determines the angular momentum transfer in a star-disk system. Simulations including SDMI have been reported in works by Romanova et al. (2009, 2013) with the code which is not publicly available, and ZF09 and Zanni & Ferreira (2013)

with the publicly available code PLUTO (v.3). Following ZF09, I perform simulations with the updated version of the PLUTO code (v.4.1) (Mignone et al. 2007, 2012).

I present a short version of the set-up, amended to facilitate reproducibility¹.

The equations solved in the magneto-hydrodynamic (MHD) module of the PLUTO code are, in the cgs system of units:

$$\frac{\partial \rho}{\partial t} + \nabla \cdot (\rho \mathbf{v}) = 0 \quad (\text{A.1})$$

$$\frac{\partial \rho \mathbf{v}}{\partial t} + \nabla \cdot \left[\rho \mathbf{v} \mathbf{v} + \left(P + \frac{\mathbf{B} \mathbf{B}}{8\pi} \right) \mathbf{I} - \frac{\mathbf{B} \mathbf{B}}{4\pi} - \boldsymbol{\tau} \right] = \rho \mathbf{g} \quad (\text{A.2})$$

$$\frac{\partial E}{\partial t} + \nabla \cdot \left[\left(E + P + \frac{\mathbf{B} \mathbf{B}}{8\pi} \right) \mathbf{v} \right] \quad (\text{A.3})$$

$$+ \nabla \cdot \left[\underbrace{\eta_m \mathbf{J} \times \mathbf{B} / 4\pi - \mathbf{v} \cdot \boldsymbol{\tau}}_{\text{heating terms}} \right] = \rho \mathbf{g} \cdot \mathbf{v} - \underbrace{\Lambda}_{\text{cooling}} \quad (\text{A.4})$$

$$\frac{\partial \mathbf{B}}{\partial t} + \nabla \times (\mathbf{B} \times \mathbf{v} + \eta_m \mathbf{J}) = 0 \quad (\text{A.5})$$

where the symbols have their usual meaning: ρ and \mathbf{v} are the matter density and velocity vector, P is the pressure, \mathbf{B} is the magnetic field and η_m and $\boldsymbol{\tau}$ represent the resistivity and the viscous stress tensor, respectively. Λ is the cooling source term, the gravity acceleration is $\mathbf{g} = -\nabla \Phi_g$, where the gravitational potential of the star with mass M_* is equal to $\Phi_g = -GM_*/R$. Then $g_R = -1.0/R^2$ in the code units.

Simulations are performed using the second-order piecewise linear reconstruction, with a Van Leer limiter in density and magnetic field and a minmod limiter in the pressure and velocity. To enhance stability, in the subroutine `plm_states`, the default is set to Van Leer instead of the less diffusive monotized central difference limiter. An approximate Roe solver (hlld in the PLUTO options) is used, with a modification in the `flag_shock` subroutine: flags are set to switch to more diffusive hll solver if the internal energy is less than 1% of the total energy, instead of switching in the presence of shocks. The second-order time-stepping (RK2) is employed, and $\nabla \cdot \mathbf{B} = 0$ is maintained by the Constrained Transport. The magnetic field is evolved with the split-field option, so that only changes from the initial stellar magnetic field are evolved in time (Tanaka 1994; Powell et al. 1999). In version 4.1 of PLUTO the Constrained Transport is by default disabled to work with the background field in the resistive MHD-it is probably an artifact from the older version. To enable the background field option, the constraint is removed by changing the condition in the routine `backgrnd_field`, to point to some feature which will not be used, e.g. thermal conduction.

A logarithmically stretched radial grid, and uniform grid in the meridional half-plane $\theta = [0, \pi/2]$ in spherical coordinates are used to perform 2D-axisymmetric SDMI simulations. The resolution is set to $R \times \theta = (217 \times 100)$ grid cells, in the physical domain from the stellar surface to 30 stellar radii, as shown in Fig. A.1.

¹ Author is aware of several unsuccessful attempts in repeating the ZF09 set-up by experienced researchers and students during the last decade. To my knowledge, the first successful following has been reported in Čemeljić et al. (2017).

The total energy density is $E = P/(\gamma-1) + \rho(\mathbf{v} \cdot \mathbf{v})/2 + \mathbf{B} \cdot \mathbf{B}/8\pi$, where $\gamma = 5/3$ is the plasma polytropic index. The electric current is given by the Ampere's law $\mathbf{J} = \nabla \times \mathbf{B}/4\pi$.

To prevent the thermal thickening of the accretion disk in simulations, following ZF09 description, from the PLUTO energy equation the underbraced Ohmic and viscous heating terms are removed. This equals to the assumption that all the heating is radiated away from the disk. To do this, lines in the code with the viscous and resistive part of the fluxes computation in `parabolic_flux` subroutine are commented out. The viscous and resistive fluxes are added in the `rhs` subroutine, to ensure the inclusion of the correct dissipative fluxes terms. Such simulations remain in the non-ideal MHD regime because of the viscous term in the momentum equation, and the resistive term in the induction equation².

The initial disk is set with the initial density set by KK00 with a self-similar profile with an aspect ratio ϵ :

$$\rho_d = \rho_{d0} \left\{ \frac{\gamma-1}{\gamma\epsilon^2} \left[\frac{R_*}{R} - \left(1 - \frac{\gamma\epsilon^2}{\gamma-1} \right) \frac{R_*}{R \sin \theta} \right] \right\}^{1/(\gamma-1)} =$$

$$= \rho_{d0} \left\{ \frac{2}{5\epsilon^2} \left[\frac{R_*}{R} - \left(1 - \frac{5}{2}\epsilon^2 \right) \frac{R_*}{R \sin \theta} \right] \right\}^{3/2}.$$
(A.6)

The pressure is

$$P_d = \epsilon^2 \rho_{d0} v_{K*}^2 \left(\frac{\rho_d}{\rho_{d0}} \right)^\gamma =$$

$$= \epsilon^2 \left[\frac{R_*}{R} - \left(1 - \frac{\gamma\epsilon^2}{\gamma-1} \right) \frac{R_*}{R \sin \theta} \right]^{5/2}.$$
(A.7)

The capital R indicates the spherical radius, and $r = R \sin \theta$ is the cylindrical radius. The disk unit density ρ_{d0} and Keplerian speed V_{K*} are both calculated in the disk midplane at R_* . The initial disk is truncated about the corotation radius.

The obtained disk is a polytropic hydrodynamical solution of the viscous accretion disk in the full 3D, obtained by approximate expansion up to the second order in the terms of $\epsilon = c_s/v_K$, the disk aspect ratio measured on the midplane of the disk, where $c_s = \sqrt{P_d/\rho_d}$ and v_K are the isothermal sound speed and the Keplerian speed in the disk.

The viscosity and resistivity are defined explicitly in separate subroutines, by a second-order finite difference approximation for the dissipative fluxes, with checking of the time step. Both are parameterized by the Shakura-Sunyaev prescription as $\alpha c^2/\Omega$. To avoid the issues related to the backflow in the disk, here is addressed only the case with $\alpha_v = 1$. The viscosity is defined by $\eta_v = \frac{2}{3}\rho\alpha_v P_0 r^{3/2}$, where P_0 is the initial pressure in the disk. The resistivity is $\eta_m = \frac{2}{5}\alpha_m P_0 r^{3/2}$. The diffusive parameters α_v and α_m are defined in separate subroutines `visc_nu` and `res_eta`. A condition for inclusion of the diffusive term is in both routines defined by the $\beta = P_{\text{mag}}/P_{\text{hyd}} > 0.5$, meaning that the magnetic pressure is prevailing. In both subroutines, the diffusive term is taken into account only when tracer value is unity, otherwise it is set to zero.

² Without modification of the energy equation, but with the power law cooling introduced to account for the disk dissipative heating, a similar outcome is obtained. It is advisable to use this, simpler method, in the first attempt of the set-up.

The initial disk velocity profile is, by KK00:

$$v_{Rd} = -\alpha_v \epsilon^2 \left[10 - \frac{32}{3} \Lambda \alpha_v^2 - \Lambda \left(5 - \frac{1}{\epsilon^2 \tan^2 \theta} \right) \right] \sqrt{\frac{GM_*}{R \sin^3 \theta}}$$
(A.8)

$$v_{R\varphi} = \left[\sqrt{1 - \frac{5\epsilon^2}{2}} + \frac{2}{3} \epsilon^2 \alpha_v^2 \Lambda \left(1 - \frac{6}{5\epsilon^2 \tan^2 \theta} \right) \right] \sqrt{\frac{GM_*}{R \sin \theta}}$$

where

$$\Lambda = \frac{11}{5} / \left(1 + \frac{64}{25} \alpha_v^2 \right).$$
(A.9)

The initial corona is a non-rotating, polytropic corona with $\gamma = 5/3$, in the hydrostatic balance. It is defined by the density and pressure given by:

$$\rho_c = \rho_{c0} (R_*/R)^{1/(\gamma-1)},$$
(A.10)

$$P_c = \rho_{c0} \frac{\gamma-1}{\gamma} \frac{GM_*}{R_*} \left(\frac{R_*}{R} \right)^{\gamma/(\gamma-1)}, \text{ where } \rho_{c0} \ll \rho_{d0}$$

is the ratio between the initial coronal and disk density, set to 0.01.

The initial stellar magnetic dipole field is set with the field axis aligned with the stellar rotation axis. There is no resistivity in the magnetosphere outside of the disk. It means that the reconnection of the magnetic field is a numerical, not physical dissipation.

In the **internal boundary** part, which enables change in the quantities inside the computational domain in PLUTO, the density in the grid cell just above the star is corrected when it falls below some limit value (I set it to 5×10^{-8}), to avoid too small density near the star. The pressure is corrected in such a way to conserve the same sound speed in the corona. To maintain the self-consistency, velocities are also changed, to conserve the momentum. Here is also ensured that the scalar tracer value is always set to zero in the corona. Around the reconnection sheet and outflows, the tracer scalar can obtain spurious values, here it is prevented.

The numerical heating in the corona is prevented by enforcing the conservation of the entropy S , to keep the values close to the initial conditions. The maximum of the entropy is atop the star, so it is kept throughout the computational box below the value $S_{\text{max}} = P_c/\rho_c^\gamma = 2\rho_{c0}^{-2/3}/(5R_*) = 8.61774$. For the minimum, the small number $S_{\text{min}} = 0.01$ is set. From this are obtained corrected values for the pressure interval in the computational box, by $P = \max[\min(P, S_{\text{max}}\rho^\gamma), S_{\text{min}}\rho^\gamma]$.

In the **inner boundary conditions**, the density, pressure and toroidal components of the velocity and magnetic field are prescribed from the active zones into the boundary. The linear extrapolation is used, with Van Leer limiter in the density and the magnetic field, and minmod limiter in the pressure and velocity. For the numerical stability in the corona, in the cases with $v_R > 0$, introduced is a correction of the pressure by a free parameter T_f in the inner radial boundary condition. It should be set to the number of order a few hundred. It adjusts the ram pressure ρv^2 atop the star (stellar wind) from the default $T_f = 2v_R^2/5$ to $T_f = (2/5 - T_f) * v_R^2$ so that the pressure in the corona is given by $P = (2/5 - T_f * v_R^2) \rho_c R_i^{-5/2}$. The first term here is the coronal initial pressure $P_c = 2\rho_c R_i^{-5/2}/5$. Since

$P \sim \rho T$ in the ideal gas law, we can think of $2/5$ as an effective temperature, where T_f is an ad-hoc correction.

In the axisymmetric 2D set-up, only the toroidal component of the magnetic field is set in the staggered grid, because in the Constrained Transport method, a staggered grid is used³. I use a specially tailored boundary condition for B_φ , in which $\Omega_{\text{eff}} = \Omega - v_p B_\varphi / r B_p$ is derived from the condition for the stellar surface as a rotating perfect conductor. The magnetic torque to drive the plasma rotation atop the star is set, with the matching measured by the comparison of the stellar angular velocity and the effective rotation rate of the field lines by the ratio $\Omega_{\text{eff}}/\Omega_*$. This prescribes rotation of the matter atop the star and the effective rotation rate of the field lines to Ω_{eff} , with v_p and B_p standing for the poloidal velocity and magnetic field, respectively. In addition, in the Constrained Transport method subroutine `ct_toroidal` component of the EMF is set to zero. Then in the stellar reference frame, the electric field is zero, with the flow speed parallel to the magnetic field.

I do not follow the suggestion in ZF09 to impose a continuity of the speed along the field lines on the outflowing matter, nor the continuity of the axisymmetric MHD invariant $k = 4\pi\rho v_p/B_p$ on the infalling material, as it did not show to improve the result.

With those corrections, the stellar rotation rate is set. I start the simulation with Ω_* , not with the slower rotation of the star as described in ZF09.

In the **outer boundary conditions**, in the coronal part of the domain, the logarithmic extrapolation in the density and pressure is set. In the radial and meridional components of the velocity an outflow is set, and a linear extrapolation with the minmod limiter for the azimuthal velocity component and Van Leer limiter in the toroidal magnetic field component. At the disk outer radial boundary, I introduce the initial hydrodynamical values, anticipating the thickening of the disk for 25%. Since the velocity could roll back above the thickened disk, inflow to twice the initial disk height in the corona is prevented by setting the velocities to zero. The toroidal magnetic field is linearly extrapolated with a Van Leer limiter.

The simulations are stopped after 100 stellar rotations. In some cases, the simulation stops earlier, because of a too small timestep. It is caused by the numerical instability in the rarefied corona, not because of the instability in the disk.

Appendix A.1: Normalization and physical units

Normalized equations are solved in the code. The unit length, velocity and mass are chosen with the stellar radius R_* , the Keplerian speed at the stellar surface v_{K*} and mass M_* . The time unit is then $t_0 = R_*/v_{K*}$. Time t in the results is measured in the number of stellar rotation periods P_* . The mass flux rate is measured in $\dot{M}_0 = \rho_{d0} R_*^2 v_{K*}^3$, which is the free parameter in simulation, from which is determined ρ_{d0} , the disk density. The initial coronal density is defined as a free parameter in the code, $\rho_{c0} = 0.01\rho_{d0}$. The magnetic field unit is defined by $B_0 = v_{K*}\sqrt{\rho_{d0}}$. Torque in the simulations is measured in the units of $\dot{J}_0 = \rho_{d0} R_*^3 v_{K*}^2$.

³ When the staggered grid is used, in **boundary** subroutine one has to correct the misplaced call to the user-defined boundary at the grid cell centers, to come after the assignment of the normal component of staggered \mathbf{B} , instead before it.

Table A.1. Typical values and scaling for different central objects. The mass M_* , radius R_* , period P_* and equatorial stellar magnetic field B_* are chosen, to derive the rest of the quantities. The code units should be multiplied by the factors given in the table, to apply it to different cases.

	YSOs	WDs	NSs
$M_*(M_\odot)$	0.5	1	1.4
R_*	$2R_\odot$	5000km	10km
P_*	4.6d	6.1s	0.46ms
$B_*(\text{G})$	500	5×10^5	10^8
$\rho_{d0}(\text{g/cm}^3)$	1.2×10^{-10}	9.4×10^{-9}	4.6×10^{-6}
$v_0(\text{km/s})$	218	5150	136000
$\dot{M}_0(M_\odot/\text{yr})$	5.7×10^{-7}	1.9×10^{-9}	10^{-9}
$B_0(\text{G})$	200	5×10^4	2.93×10^7

Table A.2. Position of the light cylinder as a function of stellar rotation rate in some typical cases. Stellar rotation rate is expressed in the units of stellar breakup rotation rate, and position of the light cylinder in the stellar radii, R_* .

$\Omega_*/\Omega_{\text{br}}$	$R_{lc}(\text{YSO})$	$R_{lc}(\text{WD})$	$R_{lc}(\text{NS})$
0.05	27454	1164	44
0.1	13727	582	22
0.2	6864	291	11
0.25	9151	233	8.8
0.5	2745	116	4.4
0.75	1830	78	2.9
1.0	1373	58	2.2

Simulations can be rescaled to different objects by using the scaling coefficients from the Table A.1. In the case of compact objects, one should keep in mind that the radial extension of the domain, measured from the axis of rotation, should not reach the light cylinder, $R_{lc}\Omega_* = c$, where the azimuthal velocity equals the speed of light. This limitation was not mentioned in the previous publications with SDMI, so we write distances of the light cylinder in the different cases are listed in the Table A.2.

Appendix B: “Atlas” of the results

For comparison of matter density and poloidal magnetic field distribution in the solutions, I present the results in an “Atlas”.

To clearly show the accretion column, a zoom is done into $2/3$ of the radial domain in the simulations. The extent to which disk is magnetically connected with the star is shown with a sample of the poloidal magnetic field lines, assigned with the corresponding values of the flux function.

Snapshots are shown in the quasi-stationary state in all 64 simulations. They are grouped by the increasing stellar magnetic field and rotation rates, with four panels showing the solutions with increasing resistivity.

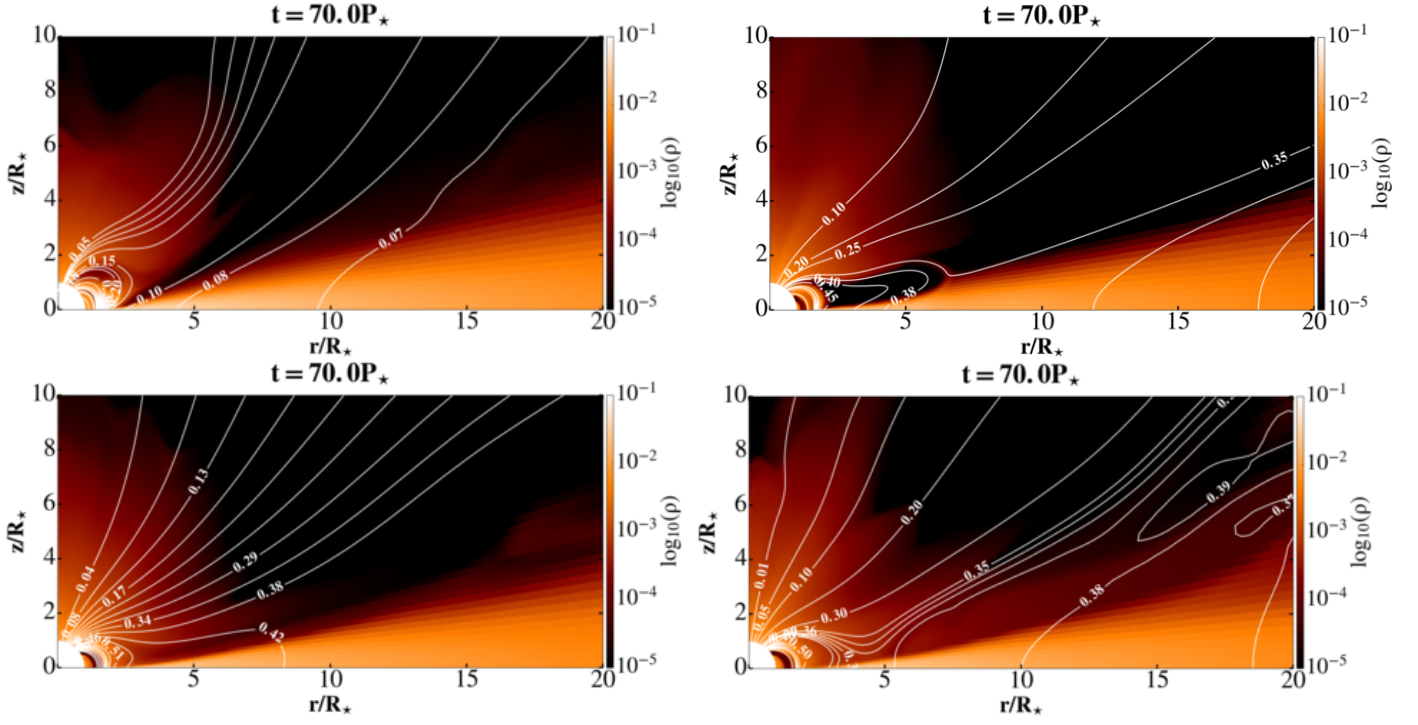


Fig. B.1. Matter density and poloidal magnetic field distribution in the quasi-stationary interval in $\mu = 0.35$ (0.25 kG) case with $\Omega_* = 0.05$, with $\alpha_m = 0.1, 0.4, 0.7$ and 1.0 .

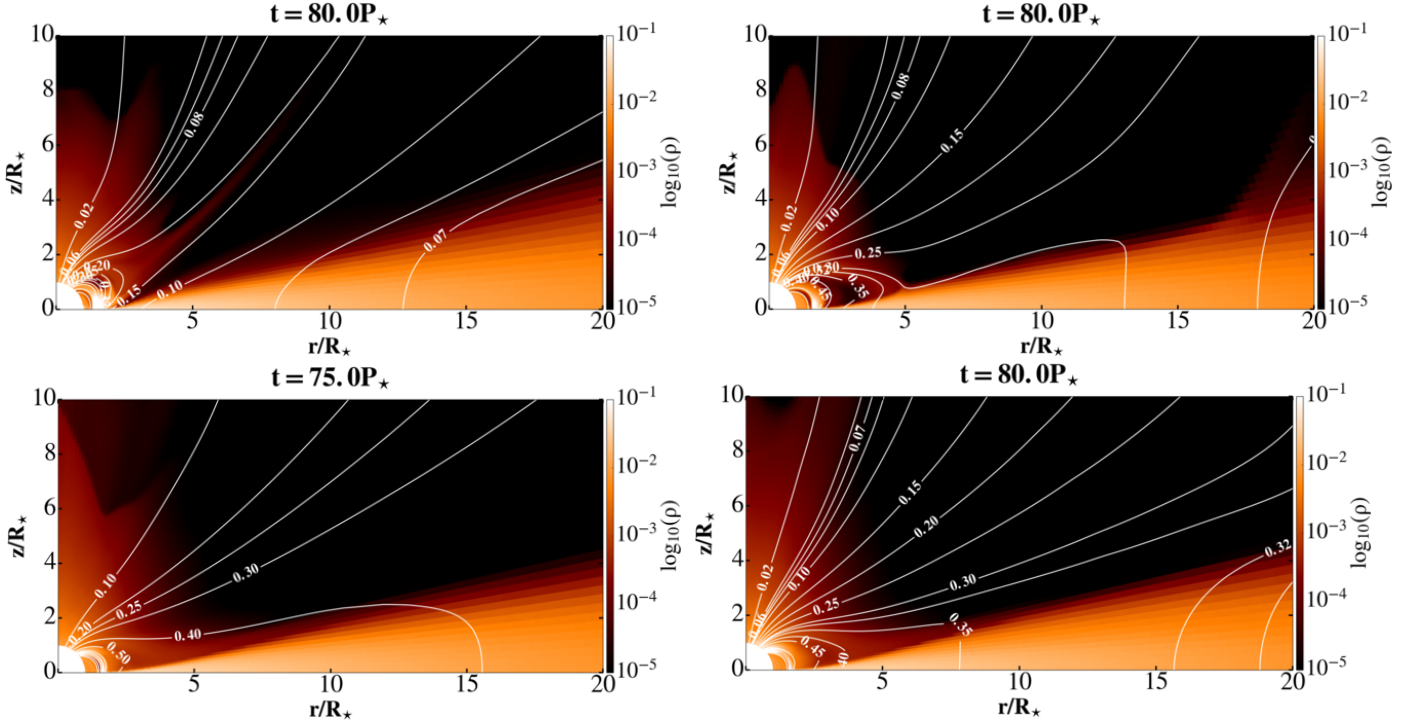


Fig. B.2. Matter density and poloidal magnetic field distribution in the quasi-stationary interval in $\mu = 0.35$ (0.25 kG) case with $\Omega_* = 0.1$, with $\alpha_m = 0.1, 0.4, 0.7$ and 1.0 .

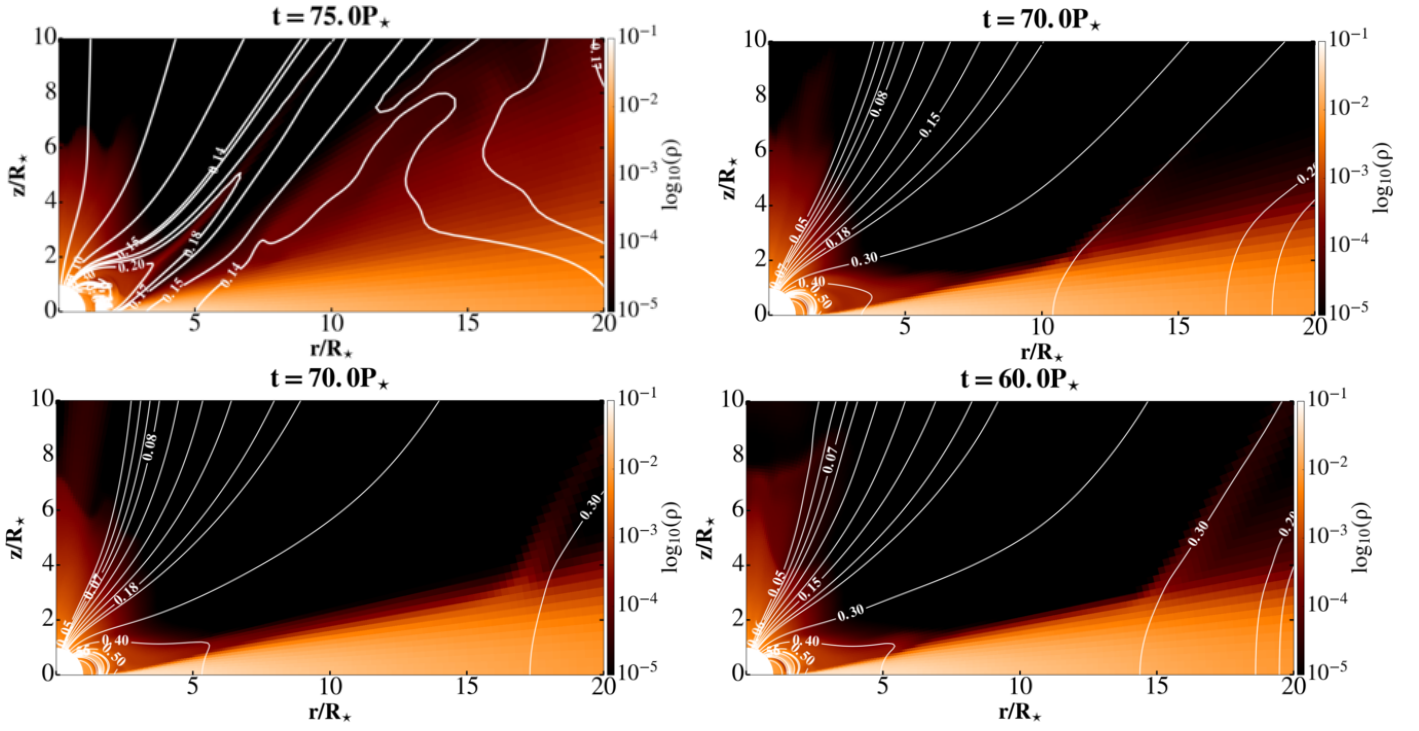


Fig. B.3. Matter density and poloidal magnetic field distribution in the quasi-stationary interval in $\mu = 0.35$ (0.25 kG) case with $\Omega_*=0.15$, with $\alpha_m = 0.1, 0.4, 0.7$ and 1.0 .

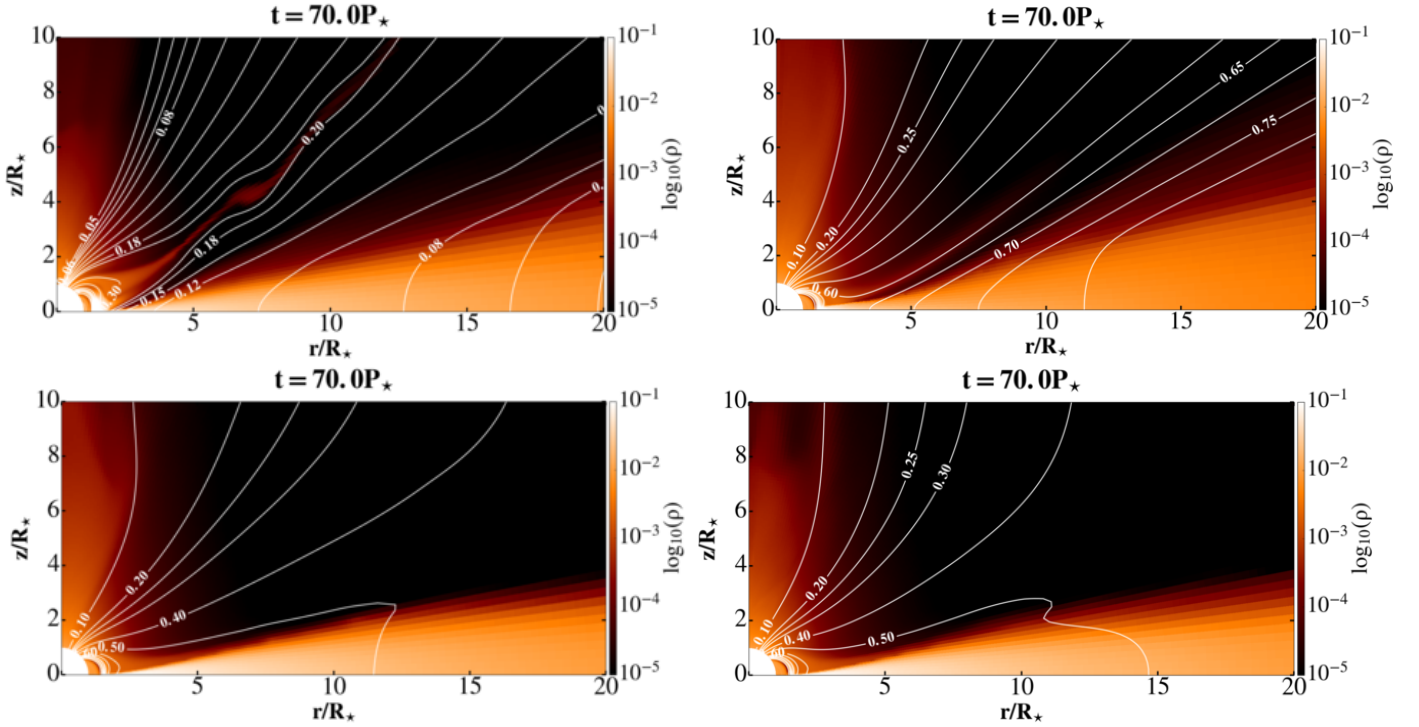


Fig. B.4. Matter density and poloidal magnetic field distribution in the quasi-stationary interval in $\mu = 0.35$ (0.25 kG) case with $\Omega_*=0.2$, with $\alpha_m = 0.1, 0.4, 0.7$ and 1.0 .

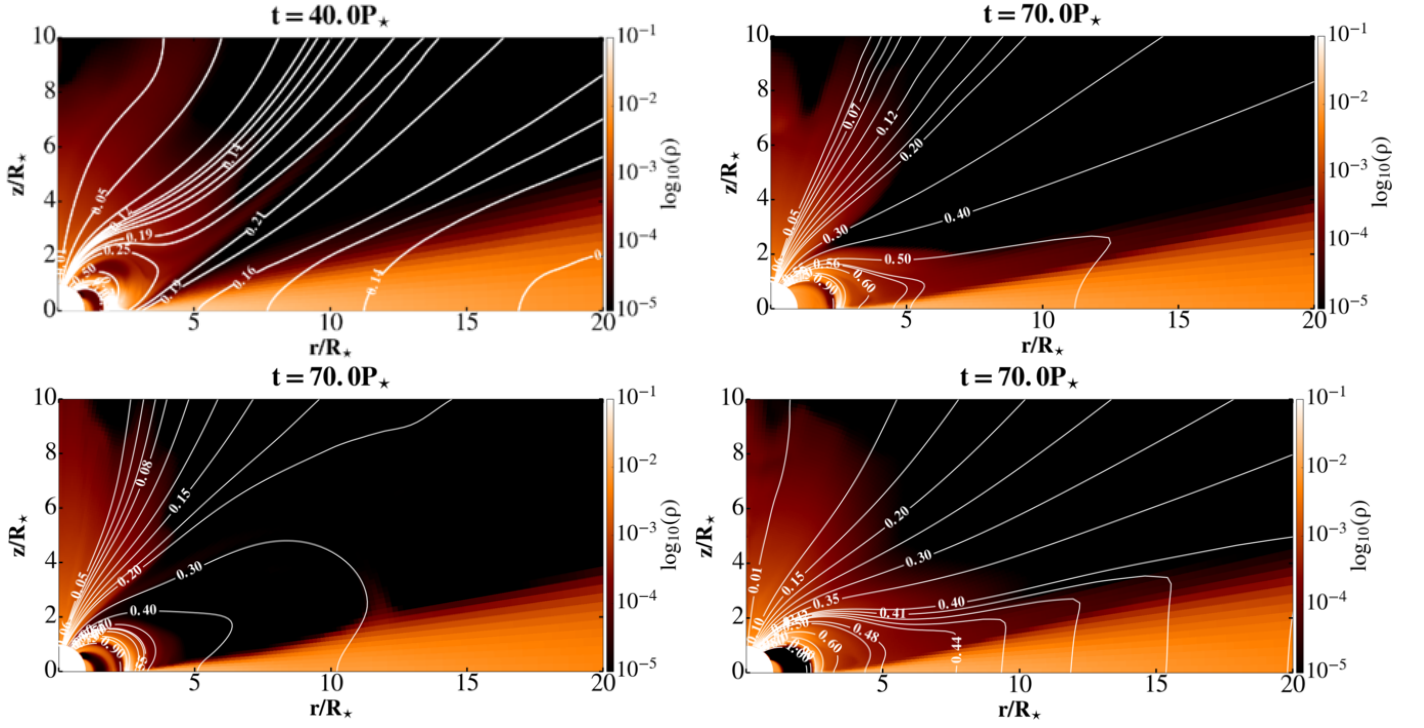


Fig. B.5. Matter density and poloidal magnetic field distribution in the quasi-stationary interval in $\mu = 0.7$ (0.5 kG) case with $\Omega_*=0.05$, with $\alpha_m = 0.1, 0.4, 0.7$ and 1.0 .

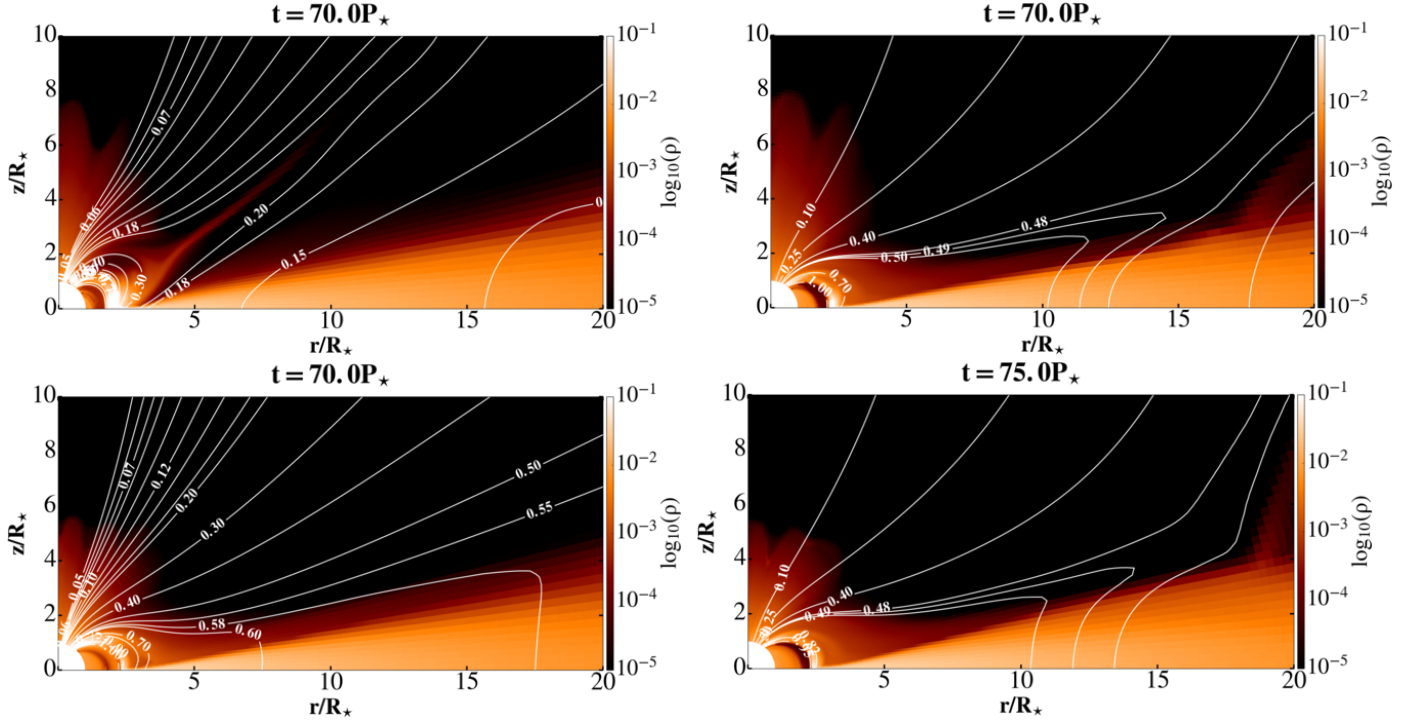


Fig. B.6. Matter density and poloidal magnetic field distribution in the quasi-stationary interval in $\mu = 0.7$ (0.5 kG) case with $\Omega_*=0.1$, with $\alpha_m = 0.1, 0.4, 0.7$ and 1.0 .

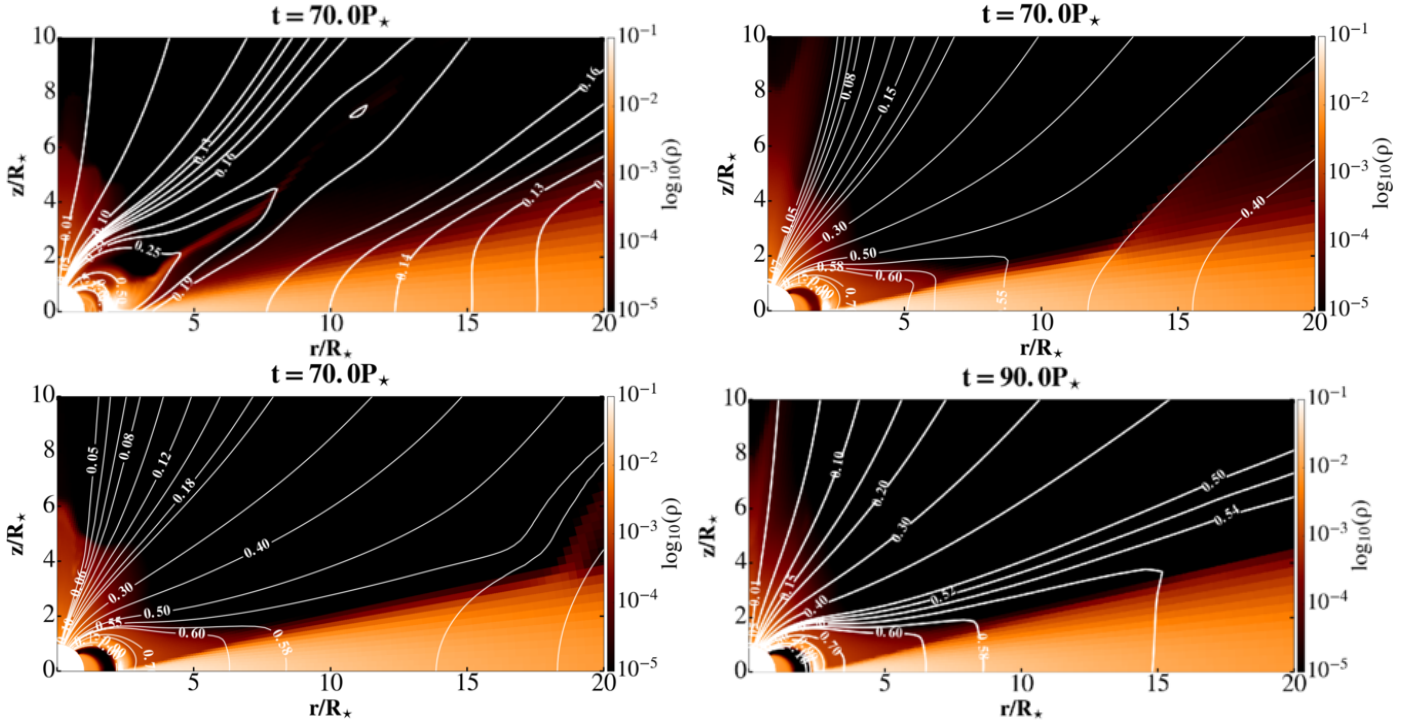


Fig. B.7. Matter density and poloidal magnetic field distribution in the quasi-stationary interval in $\mu = 0.7$ (0.5 kG) case with $\Omega_*=0.15$, with $\alpha_m = 0.1, 0.4, 0.7$ and 1.0 .

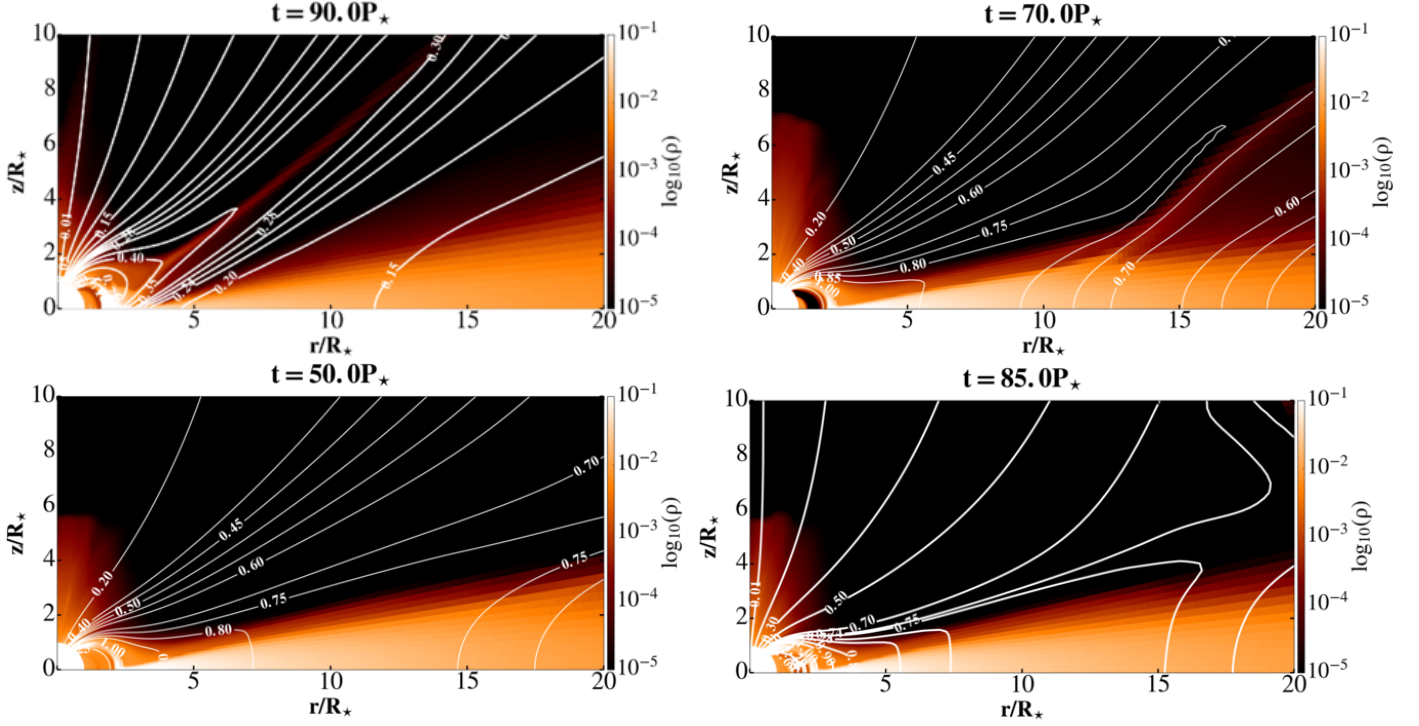


Fig. B.8. Matter density and poloidal magnetic field distribution in the quasi-stationary interval in $\mu = 0.7$ (0.5 kG) case with $\Omega_*=0.2$, with $\alpha_m = 0.1, 0.4, 0.7$ and 1.0 .

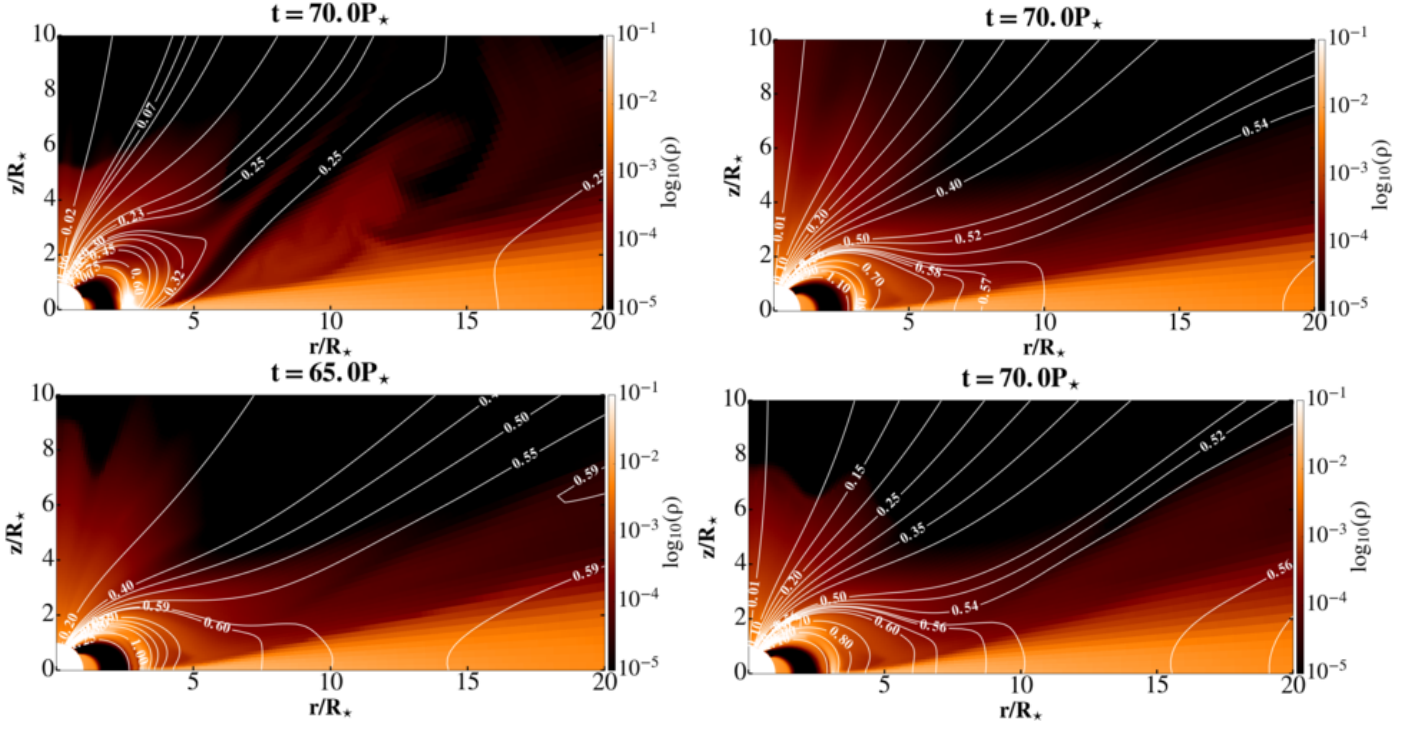


Fig. B.9. Matter density and poloidal magnetic field distribution in the quasi-stationary interval in $\mu = 1.05$ (0.75 kG) case with $\Omega_*=0.05$, with $\alpha_m = 0.1, 0.4, 0.7$ and 1.0 .

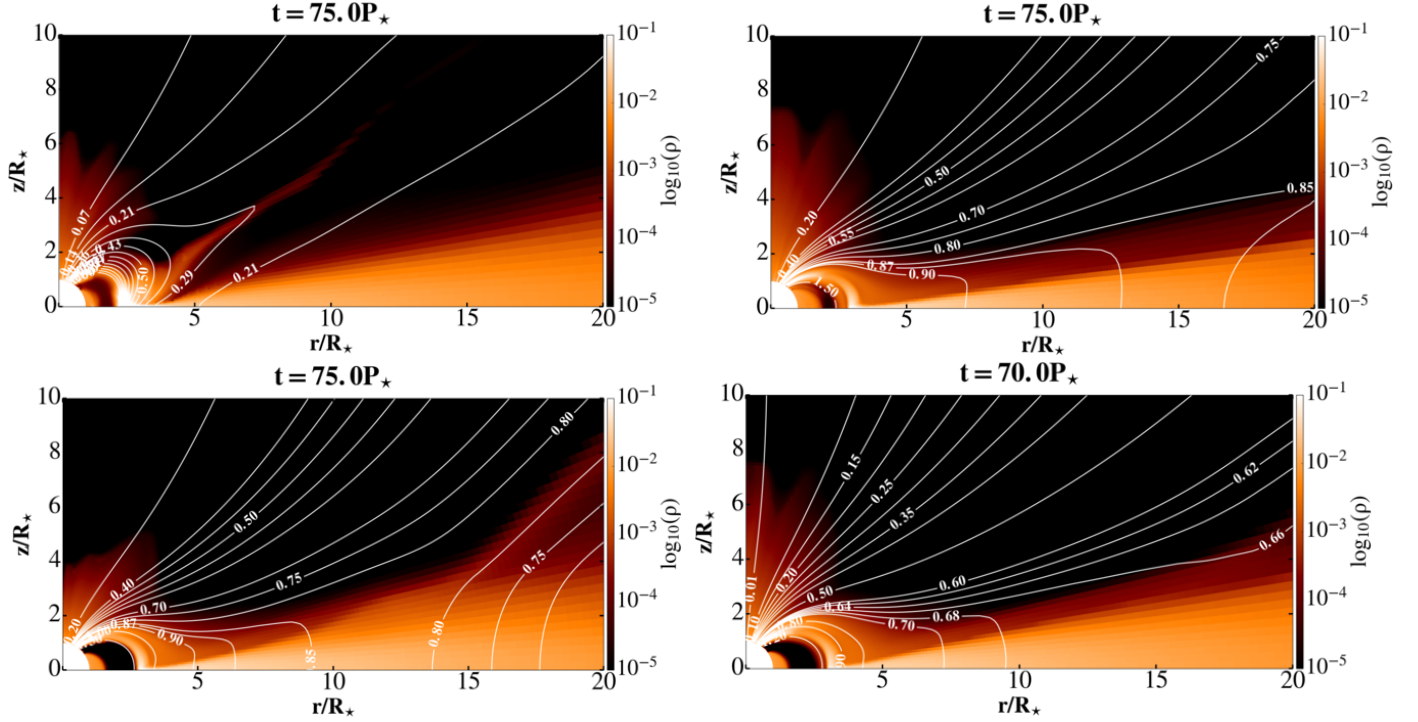


Fig. B.10. Matter density and poloidal magnetic field distribution in the quasi-stationary interval in $\mu = 1.05$ (0.75 kG) case with $\Omega_*=0.1$, with $\alpha_m = 0.1, 0.4, 0.7$ and 1.0 .

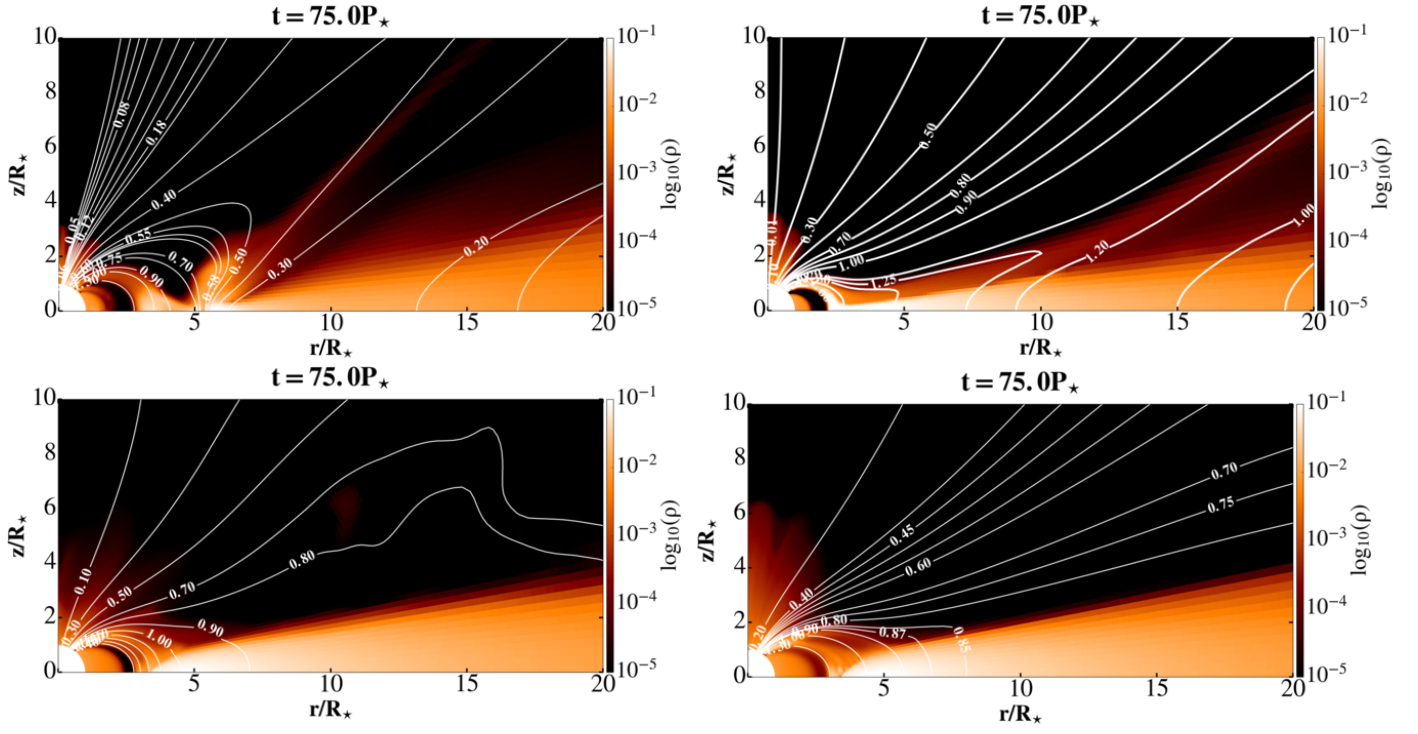


Fig. B.11. Matter density and poloidal magnetic field distribution in the quasi-stationary interval in $\mu = 1.05$ (0.75 kG) case with $\Omega_* = 0.15$, with $\alpha_m = 0.1, 0.4, 0.7$ and 1.0 .

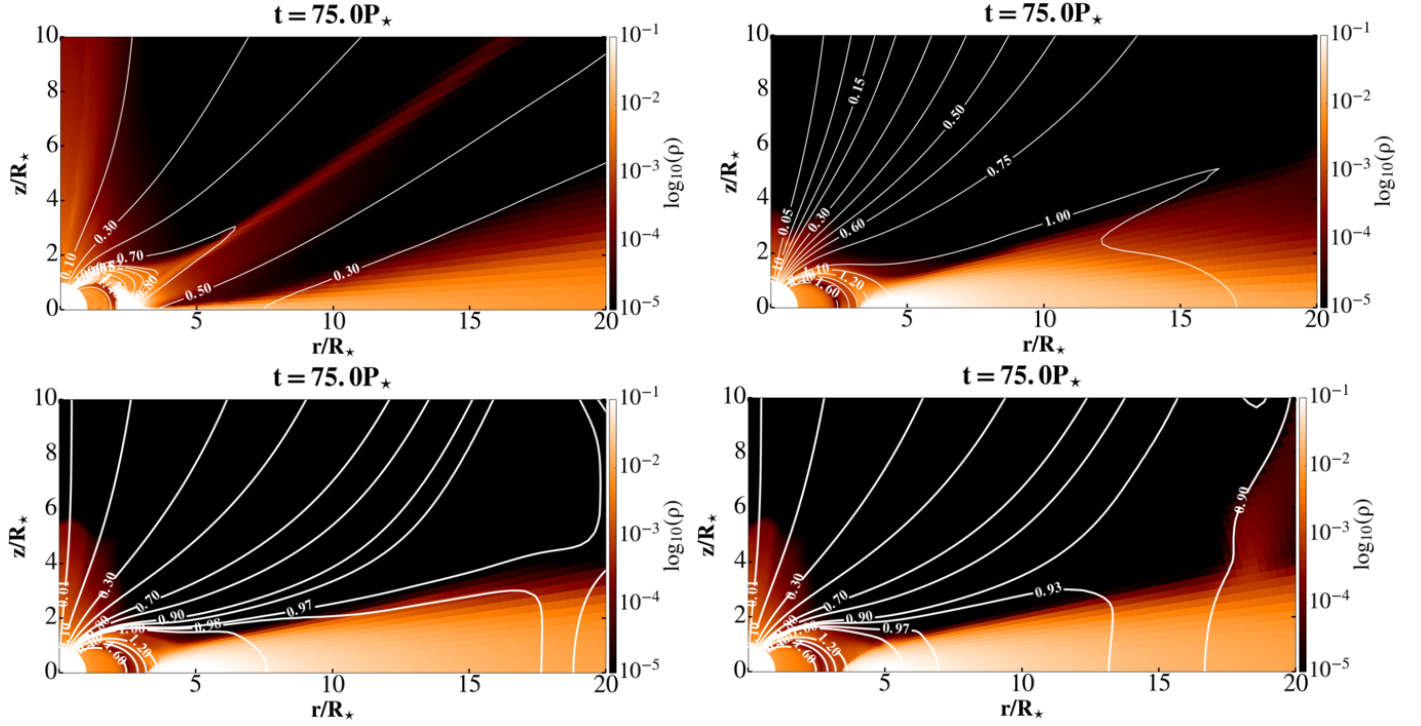


Fig. B.12. Matter density and poloidal magnetic field distribution in the quasi-stationary interval in $\mu = 1.05$ (0.75 kG) case with $\Omega_* = 0.2$, with $\alpha_m = 0.1, 0.4, 0.7$ and 1.0 .

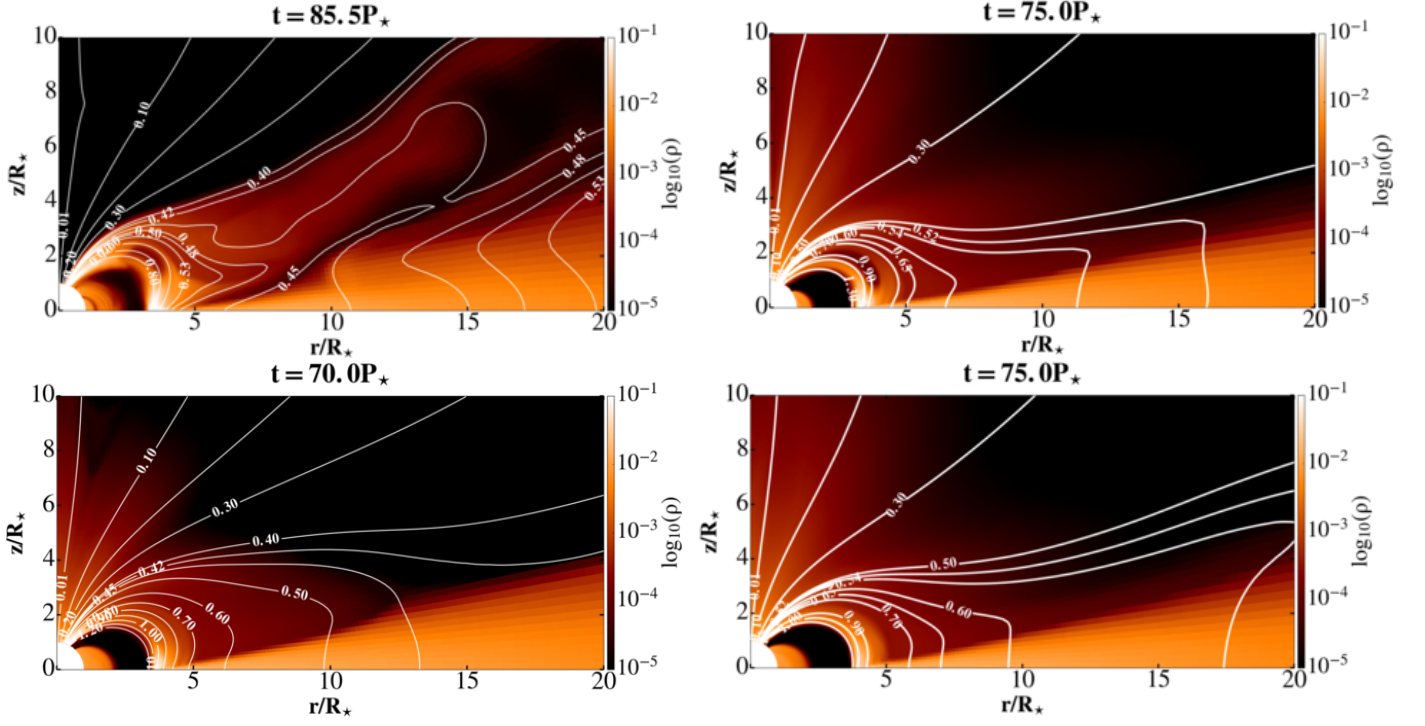


Fig. B.13. Matter density and poloidal magnetic field distribution in the quasi-stationary interval in $\mu = 1.4$ (1.0 kG) case with $\Omega_*=0.05$, with $\alpha_m = 0.1, 0.4, 0.7$ and 1.0 .

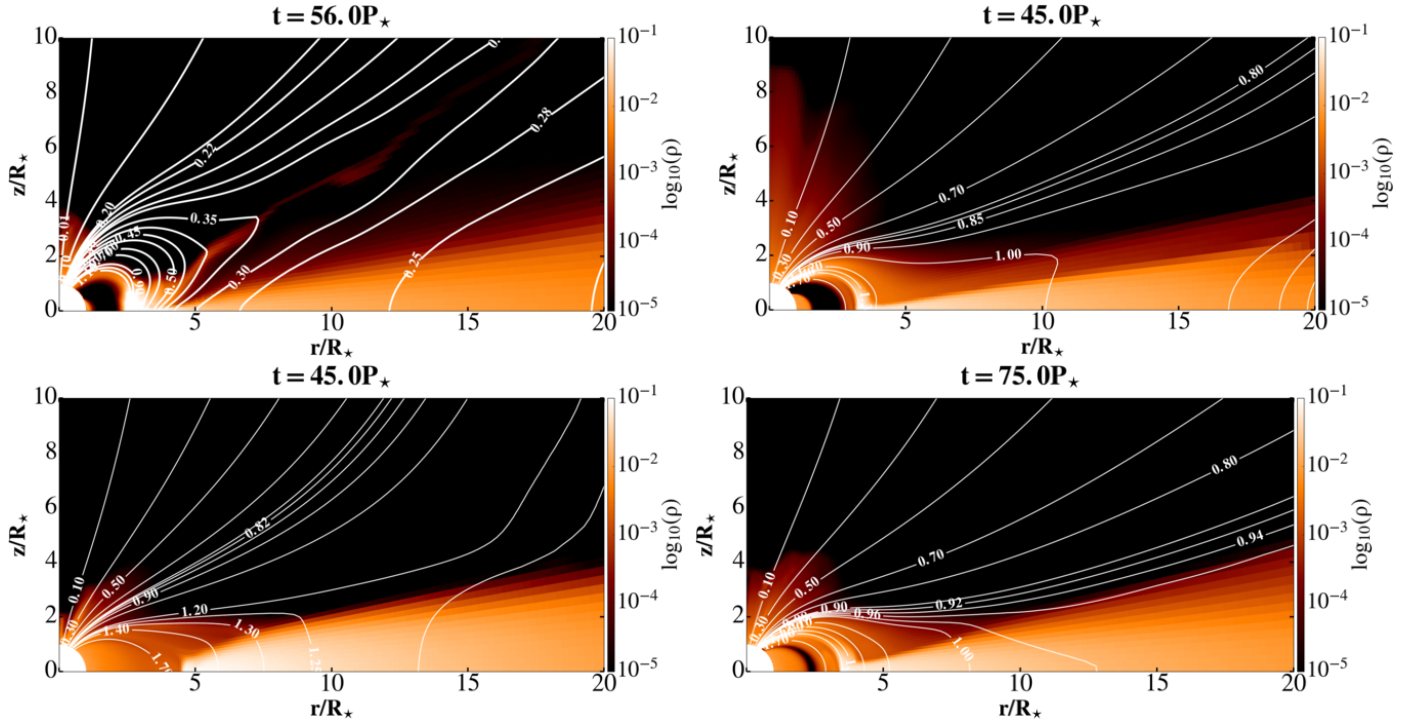


Fig. B.14. Matter density and poloidal magnetic field distribution in the quasi-stationary interval in $\mu = 1.4$ (1.0 kG) case with $\Omega_*=0.1$, with $\alpha_m = 0.1, 0.4, 0.7$ and 1.0 .

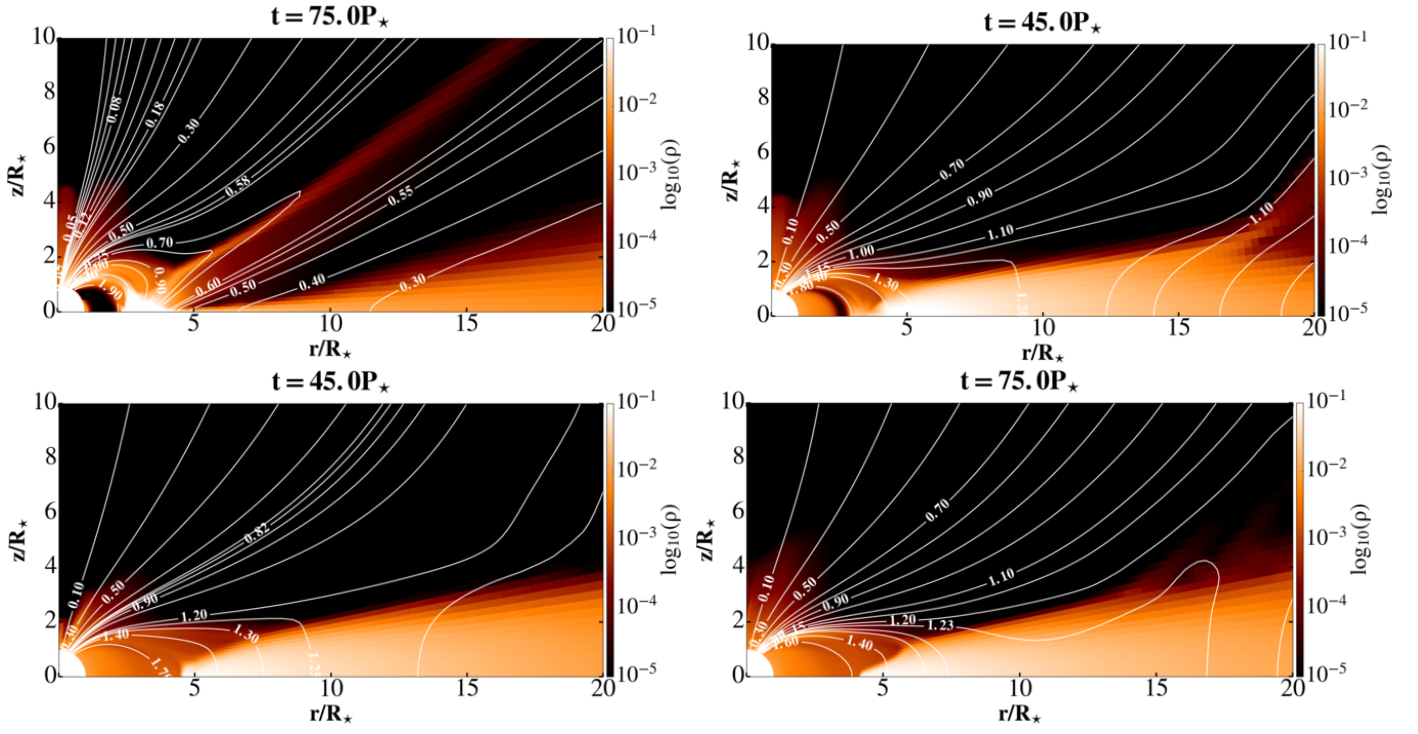


Fig. B.15. Matter density and poloidal magnetic field distribution in the quasi-stationary interval in $\mu = 1.4$ (1.0 kG) case with $\Omega_*=0.15$, with $\alpha_m = 0.1, 0.4, 0.7$ and 1.0 .

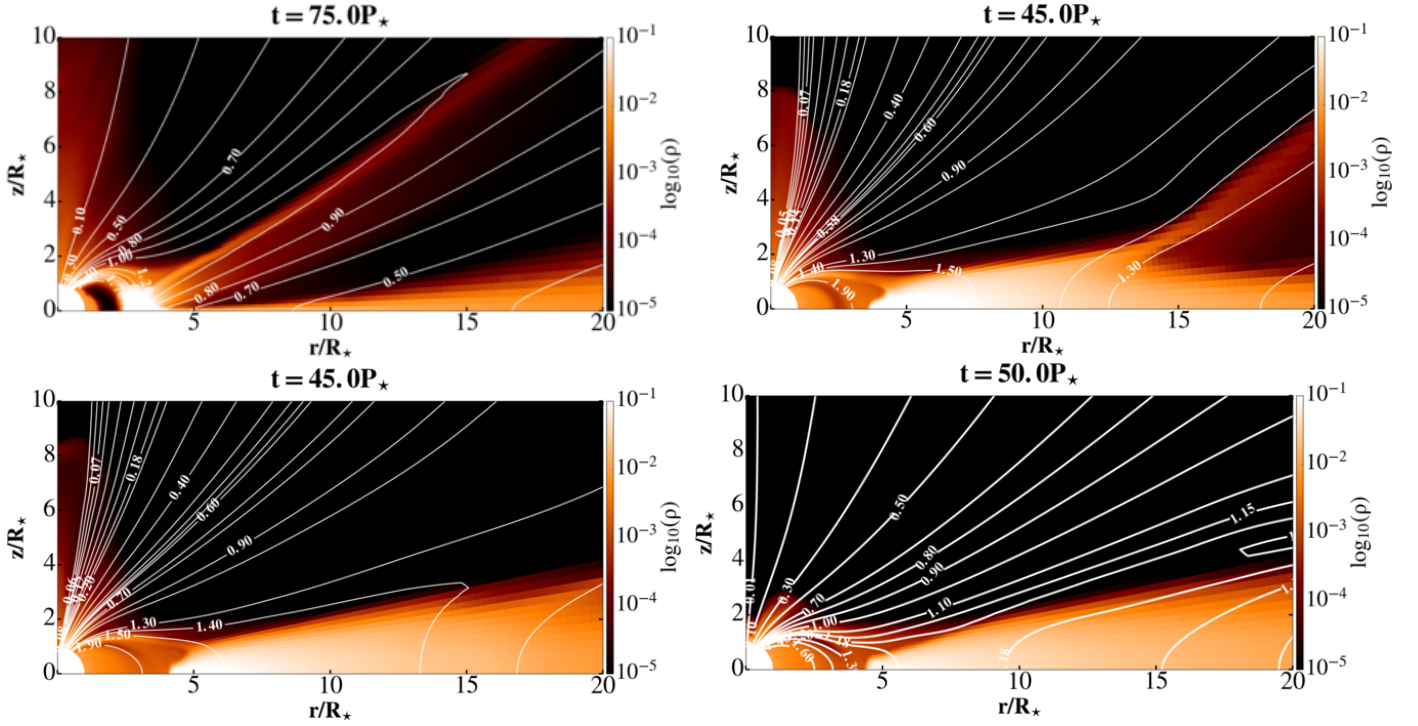


Fig. B.16. Matter density and poloidal magnetic field distribution in the quasi-stationary interval in $\mu = 1.4$ (1.0 kG) case with $\Omega_*=0.2$, with $\alpha_m = 0.1, 0.4, 0.7$ and 1.0 .